Optomechanics for thermal characterization of suspended graphene

Dolleman, Robin J.; Houri, Samer; Davidovikj, Dejan; Cartamil-Bueno, Santiago J.; Blanter, Yaroslav M.; Van Der Zant, Herre S.J.; Steeneken, Peter G.

DOI
10.1103/PhysRevB.96.165421

Publication date
2017

Document Version
Final published version

Published in
Physical Review B (Condensed Matter and Materials Physics)

Optomechanics for thermal characterization of suspended graphene

Robin J. Dolleman,* Samer Houri, Dejan Davidovikj, Santiago J. Cartamil-Bueno, Yaroslav M. Blanter, Herre S. J. van der Zant, and Peter G. Steeneken

Kavli Institute of Nanoscience, Delft University of Technology, Lorentzweg 1, 2628 CJ, Delft, The Netherlands

(Received 15 February 2017; revised manuscript received 25 July 2017; published 13 October 2017)

The thermal response of graphene is expected to be extremely fast due to its low heat capacity and high thermal conductivity. In this work, the thermal response of suspended single-layer graphene membranes is investigated by characterization of their mechanical motion in response to a high-frequency modulated laser. A characteristic delay time τ between the optical intensity and mechanical motion is observed, which is attributed to the time required to raise the temperature of the membrane. We find, however, that the measured time constants are significantly larger than the predicted ones based on values of the specific heat and thermal conductivity. In order to explain the discrepancy between measured and modeled τ, a model is proposed that takes a thermal boundary resistance at the edge of the graphene drum into account. The measurements provide a noninvasive way to characterize thermal properties of suspended atomically thin membranes, providing information that can be hard to obtain by other means.

DOI: 10.1103/PhysRevB.96.165421

I. INTRODUCTION

Graphene is a two-dimensional material with a honeycomb lattice consisting of carbon atoms [1]. Amongst its many unusual properties, its thermal conductance has attracted major attention [2,3]. Extremely high thermal conductivities have been demonstrated up to 5000 W/(m K), well exceeding the thermal conductivity of graphite [4,5]. These measurements were performed by Raman spectroscopy, that uses the temperature dependence of the phonon frequency [6]. By measuring the thermal resistance R, which is the local temperature increase ΔT per unit of heat flux ΔQ, one can employ analytical models of the heat transport to extract the thermal conductivity of graphene k. This method allowed demonstration that the thermal conductivity decreases when the number of graphene layers is increased from 2 to 4 [7]. The method has been subsequently improved, for example by better calibration of absorbed laser power [8] or removing parallel conduction paths through the air [9]. Also the amplitude ratio between Stokes and anti-Stokes signals has been exploited [10] as an alternative to the shift in phonon frequency. As an alternative to Raman measurements, electrical heaters [11], pump probe methods [12,13], scanning thermal microscopy [14], and temperature sensors [15] have been used to study heat transport in graphene, demonstrating length dependence of the thermal conductivity [11] and a reduced thermal conductivity when graphene is supported on silicon dioxide rather than freely suspended [15]. Different groups have demonstrated a large variety in thermal conductivity of pristine graphene between 2000 and 5000 W/(m K) experimentally [4,5,8–11,16–23] and between 100 and 8000 W/(m K) theoretically [22], making the thermal conductance of graphene a debated subject.

Besides these steady-state studies of the thermal properties of graphene, it is of interest to study its time-dependent thermal properties. The thermal response time of graphene is expected to be one of the fastest known, due to its low heat capacitance and high thermal conductivity. To obtain this response time, one needs to measure small temperature fluctuations in suspended graphene at frequencies in the MHz range. However, since suspended integration of temperature sensors poses problems and optical techniques for temperature measurement in suspended graphene like Raman do not offer the temperature resolution and frequency bandwidth, direct high-frequency temperature measurement in suspended graphene is difficult.

In this work, it is therefore proposed to use the thermomechanical response of suspended graphene to characterize its thermal properties at MHz frequencies. This method was previously used by Metzger et al. [24] to determine the thermal time constant τ of silicon cantilevers. Similarly, it is found that the mechanical motion of suspended graphene is delayed by a characteristic thermal time constant τ with respect to the intensity modulation of the laser that optothermally actuates the membrane. This is attributed to the time necessary for heat to diffuse through the system. The optomechanics thus provides a tool for studying the dynamic thermal properties of 2D materials. Interestingly, it is found that the measured values of τ are much higher than those expected based on literature values for the thermal conductivity k, specific heat c_p, and density ρ of graphene. Models and measurements of drums of different diameters and on different substrates are analyzed in order to account for the large value of τ. It is found that the long characteristic time can be explained by a large thermal boundary resistance at the edge of the drum.

II. EXPERIMENTAL METHODS

Single-layer graphene resonators are fabricated on top of 300-nm-deep dumbbell-shaped cavities (see Fig. 1). Two substrates are used, one with the cavities etched in a layer of silicon dioxide and the graphene directly transferred on top. The second substrate is coated with a layer of 5 nm chromium and 40 nm gold before graphene is transferred. This is done to help determine whether the thermal properties of the substrate influence the measured characteristic thermal time. Single layer graphene grown by chemical vapor deposition is transferred over both chips covered with a protective polymer.

*R.J.Dolleman@tudelft.nl

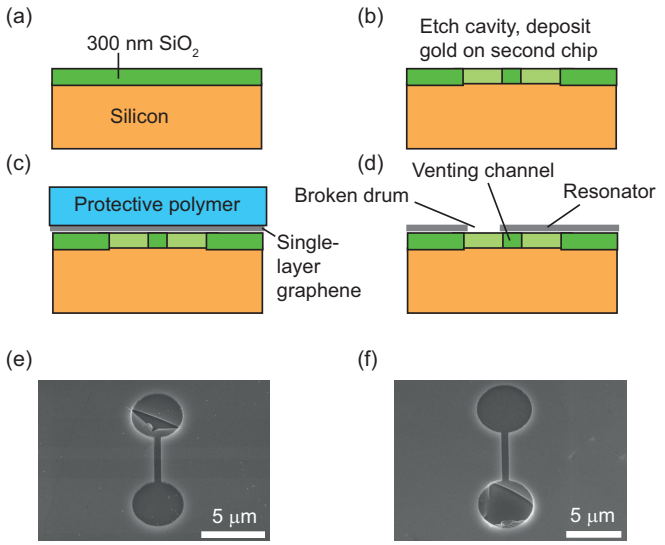

FIG. 1. Sample fabrication (a) Fabrication starts with a silicon die with 280 nm thermally grown silicon dioxide. (b) Dumbbell-shaped cavities were etched in the oxide layer. (c) Single layer graphene grown by chemical vapor deposition is transferred on both chips with a protective polymer. (d) The polymer is dissolved and the sample is dried using critical point drying. This breaks the graphene on one half of the dumbbell, creating a resonator with a venting channel on the other half. (e) Image from a scanning electron microscope (SEM) showing a successful device (3 μm diameter) with the top part broken and the bottom part whole. (f) Successful device (5 μm diameter) with the bottom part broken and the top part whole.

This polymer is dissolved and the sample is dried using critical point drying (CPD) with liquid carbon dioxide. The fluid forces in this process break one half of the dumbbell, creating a resonator on the other half with a venting channel that lets gas below the membrane escape when the vacuum chamber containing the sample is purged. The graphene is further characterized by Raman spectroscopy and atomic force microscopy (AFM) to confirm it is single layer and contamination levels are low (see Supplemental Material S1 [25]).

The interferometric setup shown in Fig. 2 is used to actuate the membrane and detect the motion [34–38]. In this setup the samples are mounted in a vacuum chamber with optical access. Graphene's motion is detected by cavity optomechanics using a red He-Ne laser, where the suspended membrane acts as a moving mirror and the bottom of the cavity as a fixed back-mirror in a low-finesse Fabry-Perot cavity. The intensity of the blue laser is modulated and heats up the membrane, which will deflect due to thermal expansion. A vector network analyzer (VNA) measures the transmission between the modulation and the signal on the photodetector in a homodyne detection scheme. Frequencies between 100 kHz and 100 MHz can be measured in this setup. All measurements are performed at pressures lower than 0.02 μbar, reducing gas damping and heat transport through the gas. The red laser power was 1.2 mW incident on the sample and the blue laser power was at 0.36 mW with a large power modulation of 67% in all experiments.

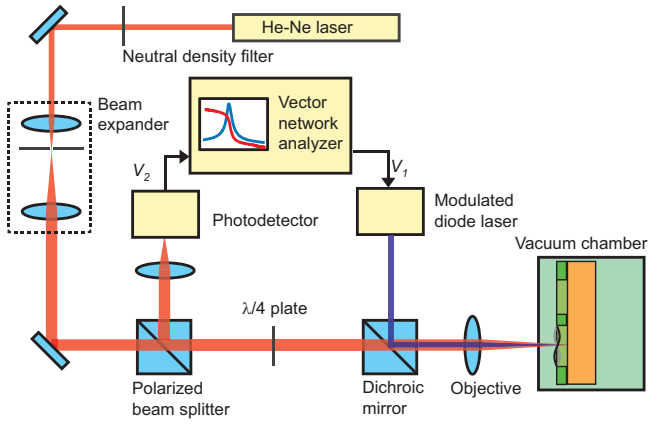

FIG. 2. Interferometry setup used to actuate and detect the motion of the resonators.

III. THERMAL TIME CONSTANT

Here we identify the potential source for time delay between the modulation of the blue laser and the mechanical response in the measurement setup. The block diagram in Fig. 3(a)

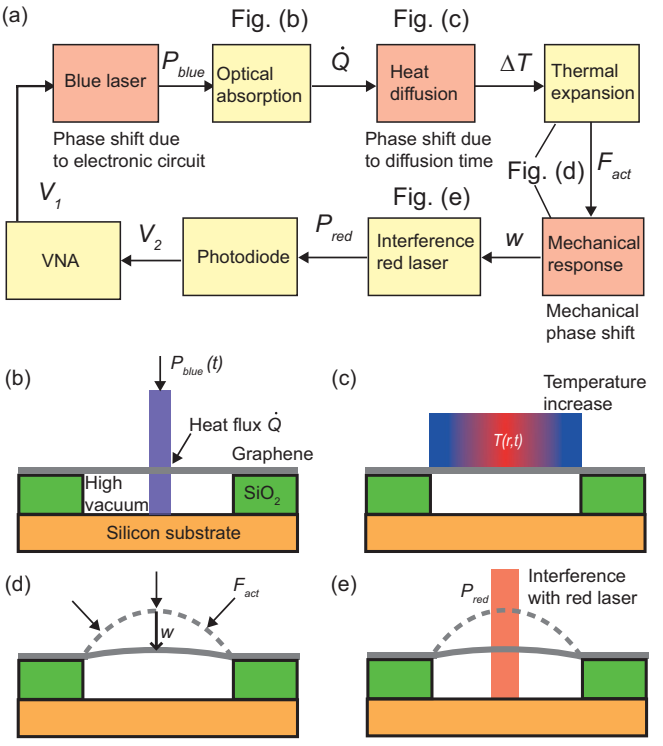

FIG. 3. Measurement method to determine the characteristic thermal time of suspended graphene resonators. (a) Block diagram showing how the deflection signal is transduced using optothermal actuation. (b) The optical power of the blue laser causes a heat flux in the graphene membrane. (c) This heat flux causes a temperature profile in the sample that depends on position and time. (d) The increased temperature in the drum causes the membrane to shrink, since graphene has a negative expansion coefficient. This results in the deflection of the graphene. (e) The deflection is detected by interference with the red laser, in which the silicon substrate acts as the fixed mirror and graphene as the moving mirror.

identifies the elements and processes that play a role in actuation and detection of the membrane's motion. The modulated intensity of the blue laser is absorbed in the graphene, generating a virtually instantaneous heating power [Fig. 3(b)] since photoexcited carriers in graphene lose their energy to phonons on time scales of a few picoseconds [39]. The generated heat will increase the temperature of the membrane and flow toward the substrate, resulting in a time-dependent temperature increase of the membrane, where the temperature is delayed with respect to the heating power [Fig. 3(c)]. The temperature increase causes thermal-expansion forces that deflect the membrane [Fig. 3(d)]. At frequencies far below the resonance frequency the motion will be in phase with the thermal-expansion force, especially since the quality factor of the resonanator is typically higher than 100. The intensity modulation of the red laser due to the interference effect that is used to detect the motion [Fig. 3(e)] can be regarded as instantaneous and will not cause a delay. The measurements are corrected for other delays, related to delays in the instruments (VNA, photodiode) and light path delays, using a calibration procedure discussed in Supplemental Material S3.

It is thus concluded that in the frequency range below the mechanical resonance, the delay between optical actuation and deflection in Fig. 3 is nearly completely due to the delay between heating power and temperature. A thermal system with a single time constant τ, driven by an ac heating power $P_{ac}e^{i\omega t}$, can be described by the heat equation

$$\frac{d\Delta T}{dt} + \frac{1}{\tau}\Delta T = \frac{P_{ac}}{C}e^{i\omega t}, \tag{1}$$

where ΔT is the temperature difference with respect to the steady-state temperature, C is the thermal capacitance, and $\tau = RC$ is the thermal RC product. At frequencies significantly below the mechanical resonance frequency, the thermal-expansion induced amplitude $z = \alpha\Delta T$ is proportional to temperature by an effective thermal-expansion coefficient α. Solution of the heat equation gives

$$z_\omega e^{i\omega t} = \alpha R P_{ac}\frac{e^{i\omega t}}{i\omega\tau + 1}. \tag{2}$$

In Sec. S6 of the Supplemental Material a full derivation of the complex amplitude z_ω, including the mechanical damping and inertia effects, is given based on derivations by Metzger et al. [24,40,41]. This equation will be used to fit the experimental data, with the parameters $B = \alpha R P_{ac}$ and τ.

IV. EXPERIMENTAL RESULTS

An example of the measured magnitude and phase of the deflection for a resonator with a diameter of 5 μm on a cavity in silicon dioxide is shown in Figs. 4(a) and 4(b) respectively. In the 0.1–10-MHz range, the response is frequency dependent with a decrease in magnitude as the frequency increases. Also a phase delay is observed that increases as a function of frequency. Note that the measured phase at low frequencies is not 0, but 180°. This is attributed to the small offset in the deflection that the graphene membrane has; in some membranes this was reversed in sign (indicated by a 0° phase at low frequencies) as shown in the Supplemental Material S2. Figure 4(c) shows a measurement result which is split into a

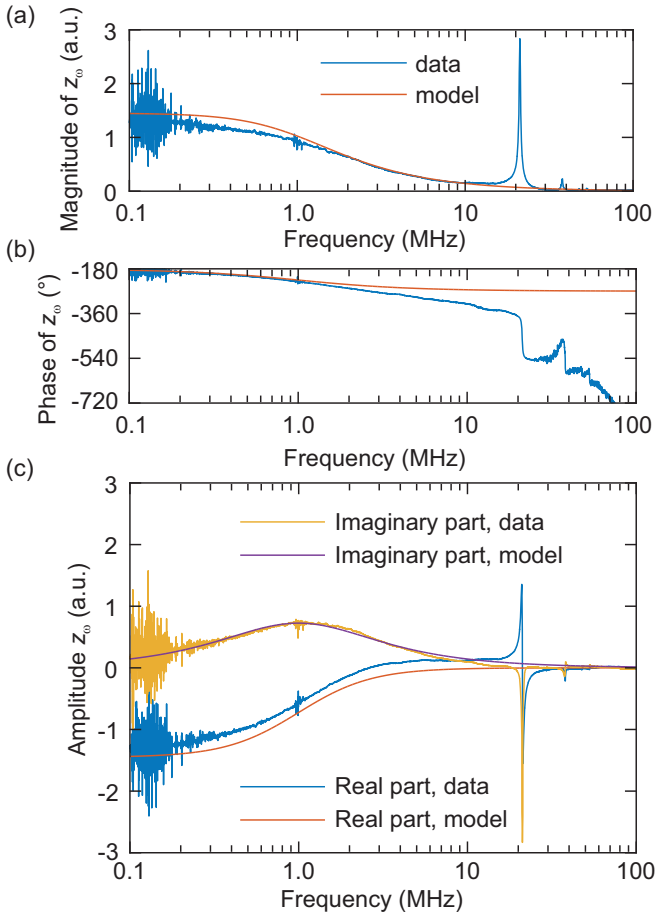

FIG. 4. Typical measured frequency response function. (a) Magnitude and (b) phase of the VNA signal after calibration, showing a decrease in magnitude and a phase shift well before the resonance frequency at 22 MHz. (c) Real and imaginary parts of the signal, with a fit from Eq. (2) to the imaginary part. The expected real part from this model is also shown in this plot.

real and an imaginary part. The imaginary part of the amplitude z_ω can be fit by Eq. (2), resulting in a value of characteristic delay time of $\tau = 159$ ns, with a clearly observable maximum at radial frequency $\omega = 1/\tau$. The real part of Eq. (2), with the same B and τ, is shown in Fig. 4(c) showing a small offset with respect to the data. The offset is attributed to optical cross talk from the modulated blue laser, which can reach the photodetector despite the optical isolation. The same effect causes the difference between the model and the magnitude and phase of the amplitude response [see Figs. 4(a) and 4(b)].

Values of τ as a function of diameter for both the silicon dioxide and the gold coated substrate are plotted in Figs. 5(a) and 5(b), respectively. Each point in the graph indicates a different drum resonator. A trend is observed where τ increases as a function of diameter. Furthermore, it is observed in Fig. 5 that there is a large variation in the value of τ for drums with the same radius. Repeated measurements of τ on the same device yield an estimated error of 8% and the scatter observed here is therefore due to device-to-device variations. Possible causes of the scatter will be discussed further below.

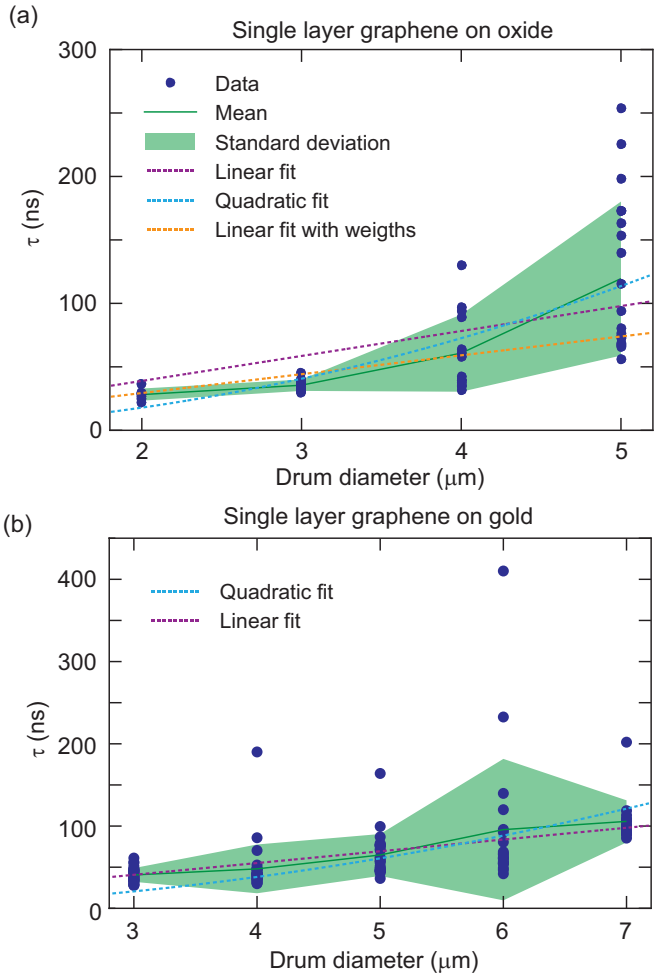

FIG. 5. Measured characteristic times compared for different diameters. Dashed lines are fits to the data in order to examine the scaling behavior of τ. (a) τ for single layer graphene suspended on a silicon dioxide substrate, showing that both τ and the spread in τ increase with diameter. (b) τ for single layer graphene drums suspended on a gold coated substrate.

V. MODELLING THE THERMAL TIME CONSTANT

The measured time constants in this work are significantly larger than expected based on the intrinsic properties of graphene. For example, Barton *et al.* [42] use an expression that estimates the time constant based on the thermal properties of graphene:

$$\tau = \frac{a^2 \rho c_p}{2k}, \tag{3}$$

where a is the membrane radius, ρ is the density of graphene, c_p is the specific heat, and k is the thermal conductivity. Using approximate values $c_p = 600$ J/(kg K) (calculated in the Supplemental Material S7), $k = 2500$ W/(m K), and $\rho = 2300$ kg/m^3 we obtain $\tau = 0.3$ ns for a 2-μm drum and $\tau = 2$ ns for a 5-μm drum. The observed values of τ range between 25 and 250 ns, which is one to two orders of magnitude larger than those predicted by Eq. (3). Even if the most extreme values for c_p and k are used, Eq. (3) gives a lower τ than measured. The theoretical limit for c_p is given by the Petit-Dulong law ($c_p = 2100$ J/kg/K), and the lowest experimental literature value for k is 600 W/(m K) [10]. Indeed a quadratic fit to the values of τ in Fig. 5 gives $k = 36$ W/(m K) for graphene on silicon dioxide and $k = 66$ W/(m K) on gold. It thus appears that Eq. (3) cannot account for the experimental τ.

We first consider the possibility that the thermal conduction is limited by the substrate that supports the graphene resonator. In order to investigate this, we compare the results obtained on gold-coated and uncoated substrates. It is found that the τ on the different substrates are similar [Figs. 5(a) and 5(b)], despite the much higher thermal conductivity of the gold-coated substrate. It is thus concluded that substrate effects are not responsible for the observed value of τ. This conclusion is consistent with finite-element simulations (Supplemental Material S5) of the system.

It is well known that a thermal resistance can be present at the interface between two solids [43–48]. This effect is called interfacial thermal (or Kapitza) resistance and is caused by differences in the phonon velocities, which leads to scattering that limits the phonon transport across the interface. Several works have predicted interfacial resistances in graphene using molecular-dynamics simulations [49,50]. Between suspended and supported graphene a value of the boundary conductance of 2×10^{10} W/(K m^2) was reported [50]. Also, grain boundaries in graphene have been shown to cause an interfacial thermal resistance [51]. Below we argue that an interfacial thermal resistance between supported and suspended graphene could account for the unexpectedly long thermal delay times we measured.

The boundary resistance will cause the formation of a temperature discontinuity at the interface between suspended and supported graphene that can be modeled by Fourier's law [44]:

$$Q_B = \frac{T_{\text{sus}} - T_{\text{sup}}}{R_B} \equiv G_B(T_{\text{sus}} - T_{\text{sup}}), \tag{4}$$

where Q_B is the boundary heat flux, T_{sus} is the temperature in the suspended part of the graphene, and T_{sup} is the temperature of the supported part. R_B is the thermal boundary resistance and G_B is the thermal boundary conductance. In order to estimate G_B we use a thermal RC model, where the thermal time τ is given by the product of the heat capacity of suspended graphene C and the thermal resistance R. It is assumed that R is dominated by the interfacial thermal resistance R_B, such that τ becomes independent of k of graphene:

$$C = c_p \rho h_g \pi a^2, \tag{5}$$

$$R = (G_B h_g 2\pi a)^{-1}, \tag{6}$$

where h_g is the thickness of single layer graphene. Combining both expressions yields for the thermal time τ

$$\tau = \frac{\rho c_p a}{2G_B}. \tag{7}$$

This model thus predicts a linear dependence between τ and a, which is clearly different from Eq. (3). A linear fit to the data yields good agreement for graphene on gold [Fig. 5(b)]. In the case of graphene on silicon dioxide [Fig. 5(a)], a weighted linear fit to the lower values of τ produces better results, due

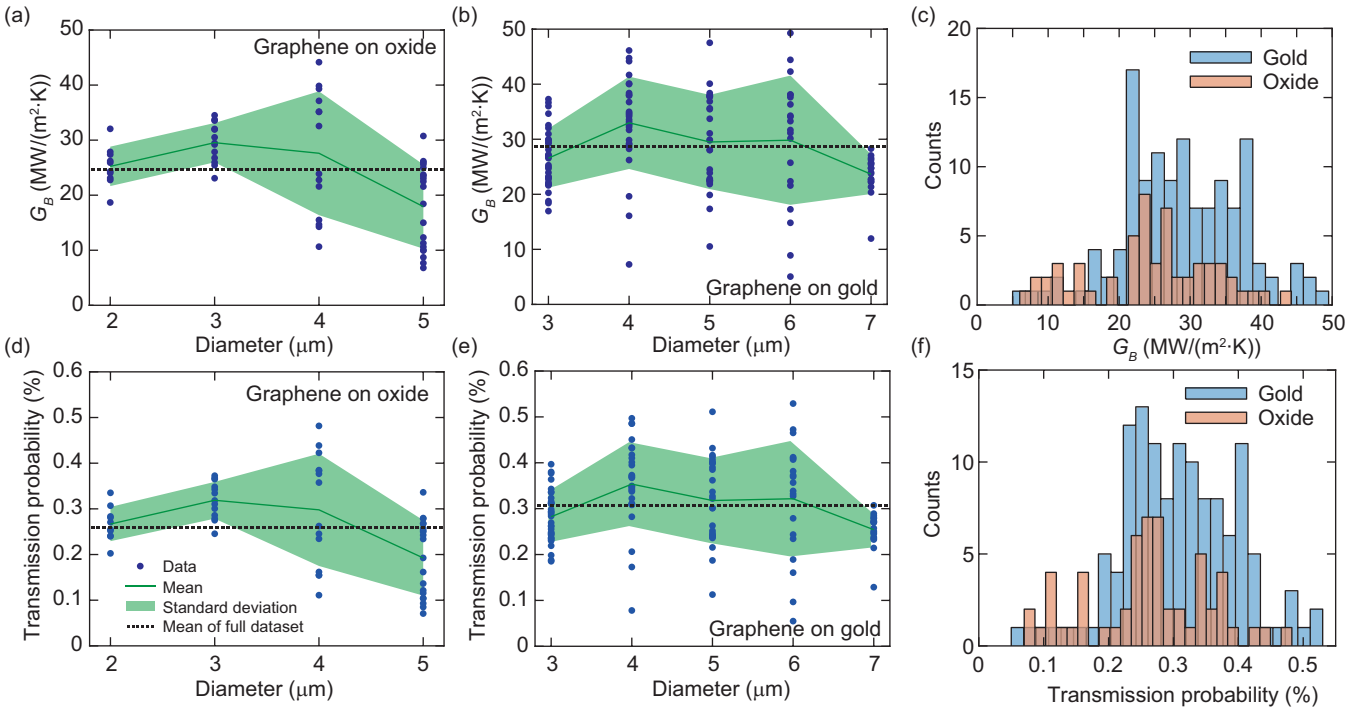

FIG. 6. Properties of the thermal boundary extracted from the measurements. (a) Thermal boundary conductance G_B extracted using Eq. (7) as function of diameter for the oxide sample and (b) for the sample covered with gold. (c) Histogram comparing all measured conductances showing the similar distributions between both the oxide and gold datasets. (d) Transmission probability from the supported to the suspended part of graphene for the oxide and (e) for the gold sample. (f) Histogram showing all obtained transmission probabilities.

to the large scatter in the 4- and 5-μm-diameter drums. The slopes of the weighted fit on silicon dioxide and the fit on gold yields nearly identical slopes within 5% of each other. Furthermore, the linear fits all fall within the error determined by the spread in τ, while the quadratic fit predicts too low values of τ for small diameters. From the slope of the linear fits, we estimate that the boundary conductance lies near $G_B = 24\ \mathrm{MW/(m^2\,K)}$.

To obtain a more accurate values of G_B, we use Eq. (7) and derive the thermal boundary conductance ($G_B = \rho c_p a/2\tau$) from the measurements of τ for each individual device as shown in Figs. 6(a)–6(c). This shows that the value of the thermal boundary conductance lies around 30 $\mathrm{MW/(m^2\,K)}$. For the purpose of extracting G_B the derived value $c_p = 600\ \mathrm{J/(kg\,K)}$ is used and a density of $\rho = 2300\ \mathrm{kg/m^3}$. Equation (7) has been verified using finite-element simulations that include a thermal boundary conductance, confirming the validity of neglecting the heat conductance k (Supplemental Material S5).

In order to relate the derived value of G_B to the phonon transmission probability across the interface, the following expression is derived in Supplemental Material S7:

$$\tau = \frac{\rho c_p a}{2G_B} = \frac{a}{2}\frac{\frac{1}{c_{1l}^2} + \frac{1}{c_{1t}^2} + \frac{\pi\hbar^2}{3\zeta(3)A_{uc}k_B^2T^2}}{\frac{\bar{w}_{1l}}{c_{1l}} + \frac{\bar{w}_{1t}}{c_{1t}} + \frac{\pi\hbar^2\bar{w}_{1z}c_{1z}}{\zeta(3)A_{uc}k_B^2T^2}}. \tag{8}$$

Here c_{1j} is the velocity of the jth phonon mode, $j = z$ for the flexural (ZA), $j = l$ for longitudinal (LA) and $j = t$ for the transverse (TA) modes. The number 1 corresponds to the suspended material. $\bar{w}_{1j}$ is the integrated transmission probability (the sum over each possible angle of incidence) of phonons over the interface, k_B is the Boltzmann constant, T is the temperature, $\hbar$ is the reduced Planck's constant, and A_{uc} is the area of the unit cell of graphene.

By using Eq. (8), an average phonon transmission probability $\bar{w}$ is plotted in Figs. 6(d)–6(f) corresponding to the boundary conductances in Figs. 6(a)–6(c). The average phonon transmission probability is found to be $\bar{w} = 0.3 \pm 0.2\%$. Potential mechanisms that limit $\bar{w}$ are discussed below.

VI. DISCUSSION

It is worth discussing whether the model proposed in Eq. (8) can account for the considerable scatter in the value of τ observed in the measurements in Fig. 5. Equation (8) shows that potential causes are differences in the phonon velocity c_{1j} or in the transmission probability w_{1j}. Temperature variations only affect the flexural phonons and are therefore expected to give too small a contribution to account for the observed scatter. Device to device variations in the transmission probability w_{1j} due to boundary roughness [52] and kinks [53] in the graphene due to sidewall adhesion [54] might play a role. In addition mechanisms that can cause phonon velocity variations between devices, like wrinkling [23], contamination [55], and the presence of grain boundaries [56] are potentially of influence. Since these mechanisms might also affect the tension in the membranes, the correlation between τ and the resonance frequency is studied (see Supplemental Material S4), however no significant

correlation is found. It is thus not possible to identify the microscopic mechanism that causes the scatter in τ from these measurements.

The tendency of the scatter in τ to increase with diameter is in accordance with Eq. (8), since τ is linearly proportional to the radius a. A notable exception to this trend is the 7-μm drums, which show significantly lower spread. Possibly this is due to a selective mechanism, due to which large wrinkled drums are eliminated by collapse on the cavity bottom [57]. In order to reduce the scatter in τ, further work on fabrication methods (e.g., transfer, growth) is needed to improve the uniformity of suspended chemical vapor deposition (CVD) graphene drums. Once the scatter is reduced, variations in device geometry can be used to further investigate the scaling laws that govern thermal time constants in graphene. This can also shed light on the role of interfacial thermal resistance and its relation to microscopic thermal mechanisms.

VII. CONCLUSIONS

To summarize, a dynamic optomechanical method to measure transient heat transport in suspended graphene is demonstrated. The method does not require electrical contacts, which allows high-throughput characterization of arrays of devices. The method is used to characterize the thermal time τ of many graphene membranes. It is found that τ is a function of diameter and its value is much larger than expected based on existing models. Measurements on gold-coated and uncoated silicon dioxide samples show similar results, showing that τ cannot be attributed to the substrate. A potential cause for the large values of τ is the presence of an interfacial thermal resistance between the suspended and supported graphene. From the measurements we determine that a thermal boundary conductance with values of 30 ± 20 MW/(m^2 K) can account for the measurements, corresponding to a low phonon transmission probability on the order of 0.3%.

ACKNOWLEDGMENTS

We thank Applied Nanolayers B.V. for supply and transfer of single-layer CVD graphene on our substrates. We also acknowledge useful discussions with T. M. Klapwijk, D. Chakraborty, D. R. Ladiges, and J. E. Sader. Further, we thank the Dutch Technology Foundation (STW, Grant No. 13307), which is part of the Netherlands Organisation for Scientific Research (NWO), and which is partly funded by the Ministry of Economic Affairs, for financially supporting this work. The research leading to these results also received funding from the European Union's Horizon 2020 research and innovation program under Grant Agreement No. 649953 Graphene Flagship and this work was supported by the Netherlands Organisation for Scientific Research (NWO/OCW), as part of the Frontiers of Nanoscience program.

[1] A. K Geim and K. S. Novoselov, The rise of graphene, Nat. Mater. **6**, 183 (2007).

[2] E. Pop, V. Varshney, and A. K. Roy, Thermal properties of graphene: Fundamentals and applications, MRS Bull. **37**, 1273 (2012).

[3] X. Xu, J. Chen, and B. Li, Phonon thermal conduction in novel 2d materials, J. Phys.: Condens. Matter **28**, 483001 (2016).

[4] A. A Balandin, S. Ghosh, W. Bao, I. Calizo, D. Teweldebrhan, F. Miao, and C. N. Lau, Superior thermal conductivity of single-layer graphene, Nano Lett. **8**, 902 (2008).

[5] S. Ghosh, I. Calizo, D. Teweldebrhan, E. P. Pokatilov, D. L. Nika, A. A. Balandin, W. Bao, F. Miao, and C. N. Lau, Extremely high thermal conductivity of graphene: Prospects for thermal management applications in nanoelectronic circuits, Appl. Phys. Lett. **92**, 151911 (2008).

[6] I. Calizo, A. A. Balandin, W. Bao, F. Miao, and C. N. Lau, Temperature dependence of the raman spectra of graphene and graphene multilayers, Nano Lett. **7**, 2645 (2007).

[7] S. Ghosh, W. Bao, D. L. Nika, S. Subrina, E. P. Pokatilov, C. N. Lau, and A. A. Balandin, Dimensional crossover of thermal transport in few-layer graphene, Nat. Mater. **9**, 555 (2010).

[8] W. Cai, A. L. Moore, Y. Zhu, X. Li, S. Chen, L. Shi, and R. S. Ruoff, Thermal transport in suspended and supported monolayer graphene grown by chemical vapor deposition, Nano Lett. **10**, 1645 (2010).

[9] S. Chen, A. L. Moore, W. Cai, J. W. Suk, J. An, C. Mishra, C. Amos, C. W. Magnuson, J. Kang, L. Shi, and R. S. Ruoff, Raman measurements of thermal transport in suspended monolayer graphene of variable sizes in vacuum and gaseous environments, ACS Nano **5**, 321 (2011).

[10] C. Faugeras, B. Faugeras, M. Orlita, M. Potemski, R. R. Nair, and A. K. Geim, Thermal conductivity of graphene in corbino membrane geometry, ACS Nano **4**, 1889 (2010).

[11] X. Xu, L. F. C. Pereira, Y. Wang, J. Wu, K. Zhang, X. Zhao, S. Bae, C. T. Bui, R. Xie, J. T. L. Thong, B. H. Hong, K. P. Loh, and D. Donadio, Length-dependent thermal conductivity in suspended single-layer graphene, Nat. Commun. **5**, 3689 (2014).

[12] C. Schwarz, Optomechanical, vibrational and thermal properties of suspended graphene membranes, Ph.D. thesis, Université Grenoble Alpes, 2016.

[13] H. Cabrera, D. Mendoza, J. L. Benítez, C. B. Flores, S. Alvarado, and E. Marín, Thermal diffusivity of few-layers graphene measured by an all-optical method, J. Phys. D **48**, 465501 (2015).

[14] K. Yoon, G. Hwang, J. Chung, H. Goo Kim, O. Kwon, K. D. Kihm, and J. S. Lee, Measuring the thermal conductivity of residue-free suspended graphene bridge using null point scanning thermal microscopy, Carbon **76**, 77 (2014).

[15] J. H. Seol, I. Jo, A. L. Moore, L. Lindsay, Z. H. Aitken, M. T. Pettes, X. Li, Z. Yao, R. Huang, D. Broido, N. Mingo, R. S. Rouff, and L. Shi, Two-dimensional phonon transport in supported graphene, Science **328**, 213 (2010).

[16] D. L Nika and A. A. Balandin, Two-dimensional phonon transport in graphene, J. Phys.: Condens. Matter **24**, 233203 (2012).

[17] A. A. Balandin, Thermal properties of graphene and nanostructured carbon materials, Nat. Mater. **10**, 569 (2011).

[18] J.-U. Lee, D. Yoon, H. Kim, S. W. Lee, and H. Cheong, Thermal conductivity of suspended pristine graphene measured by raman spectroscopy, Phys. Rev. B **83**, 081419 (2011).

[19] V. E. Dorgan, A. Behnam, H. J. Conley, K. I. Bolotin, and E. Pop, High-field electrical and thermal transport in suspended graphene, Nano Lett. **13**, 4581 (2013).
[20] S. Chen, Q. Wu, C. Mishra, J. Kang, H. Zhang, K. Cho, W. Cai, A. A. Balandin, and R. S. Ruoff, Thermal conductivity of isotopically modified graphene, Nat. Mater. **11**, 203 (2012).
[21] H. Li, H. Ying, X. Chen, D. L. Nika, A. I. Cocemasov, W. Cai, A. A. Balandin, and S. Chen, Thermal conductivity of twisted bilayer graphene, Nanoscale **6**, 13402 (2014).
[22] D. L. Nika and A. A. Balandin, Thermal transport in graphene, few-layer graphene and graphene nanoribbons, in *Thermal Transport in Low Dimensions*, edited by S. Lepri, Lecture Notes in Physics, Vol. 921 (Springer, cham, 2016), pp. 339.
[23] S. Chen, Q. Li, Q. Zhang, Y. Qu, H. Ji, R. S. Ruoff, and W. Cai, Thermal conductivity measurements of suspended graphene with and without wrinkles by micro-raman mapping, Nanotechnology **23**, 365701 (2012).
[24] C. Metzger, I. Favero, A. Ortlieb, and K. Karrai, Optical self cooling of a deformable fabry-perot cavity in the classical limit, Phys. Rev. B **78**, 035309 (2008).
[25] See Supplemental Material at http://link.aps.org/supplemental/10.1103/PhysRevB.96.165421 for additional graphene characterization (S1), an example of a measurement with reversed phase (S2), explanation of the calibration procedure (S3), correlation between resonance frequency and τ (S4), finite-element simulations including the substrate (S5), extended derivation of expression for motion of drum actuated by modulated laser (S6), and the derivation of expression for τ (S7). The Supplemental Material includes Refs. [26–33].
[26] P. Nemes-Incze, Z. Osváth, K. Kamarás, and L. P. Biró, Anomalies in thickness measurements of graphene and few layer graphite crystals by tapping mode atomic force microscopy, Carbon **46**, 1435 (2008).
[27] A. C. Ferrari, J. C. Meyer, V. Scardaci, C. Casiraghi, M. Lazzeri, F. Mauri, S. Piscanec, D. Jiang, K. S. Novoselov, S. Roth, and A. K. Geim, Raman Spectrum of Graphene and Graphene Layers, Phys. Rev. Lett. **97**, 187401 (2006).
[28] Z. Chen, W. Jang, W. Bao, C. N. Lau, and C. Dames, Thermal contact resistance between graphene and silicon dioxide, Appl. Phys. Lett. **95**, 161910 (2009).
[29] K. F. Mak, C. H. Lui, and T. F. Heinz, Measurement of the thermal conductance of the graphene/SiO2 interface, Appl. Phys. Lett. **97**, 221904 (2010).
[30] M. Freitag, M. Steiner, Y. Martin, V. Perebeinos, Z. Chen, J. C. Tsang, and P. Avouris, Energy dissipation in graphene field-effect transistors, Nano Lett. **9**, 1883 (2009).
[31] K. E. Gray, *Nonequilibrium Superconductivity, Phonons, and Kapitza Boundaries* (Plenum, New York, 1981).
[32] J. Hone, Phonons and thermal properties of carbon nanotubes, in *Carbon Nanotubes* (Springer, Berlin, Heidelberg, New York, 2001), p. 273.
[33] I. M. Lifshitz, Thermal properties of chain and layered structures at low temperatures, Zh. Eksp. Teor. Fiz. **22**, 475 (1952).
[34] J. S. Bunch, A. M. Van Der Zande, S. S. Verbridge, I. W. Frank, D. M. Tanenbaum, J. M. Parpia, H. G. Craighead, and P. L. McEuen, Electromechanical resonators from graphene sheets, Science **315**, 490 (2007).
[35] R. J. Dolleman, D. Davidovikj, S. J. Cartamil-Bueno, H. S. J. van der Zant, and P. G. Steeneken, Graphene squeeze-film pressure sensors, Nano Lett. **16**, 568 (2016).
[36] R. J. Dolleman, S. J. Cartamil-Bueno, H. S. J. van der Zant, and P. G. Steeneken, Graphene gas osmometers, 2D Mater. **4**, 011002 (2016).
[37] A. Castellanos-Gomez, R. van Leeuwen, M. Buscema, H. S. J. van der Zant, G. A. Steele, and W. J. Venstra, Single-layer mos2 mechanical resonators, Adv. Mater. **25**, 6719 (2013).
[38] A. M. van der Zande, R. A. Barton, J. S. Alden, C. S. Ruiz-Vargas, W. S. Whitney, P. H. Q. Pham, J. Park, J. M. Parpia, H. G. Craighead, and P. L. McEuen, Large-scale arrays of single-layer graphene resonators, Nano Lett. **10**, 4869 (2010).
[39] H. Wang, J. H. Strait, P. A. George, S. Shivaraman, V. B. Shields, M. Chandrashekhar, J. Hwang, F. Rana, M. G. Spencer, C. S. Ruiz-Vargas, and J. Park, Ultrafast relaxation dynamics of hot optical phonons in graphene, Appl. Phys. Lett. **96**, 081917 (2010).
[40] C. Höhberger Metzger and K. Karrai, Cavity cooling of a microlever, Nature (London) **432**, 1002 (2004).
[41] I. Favero, C. Metzger, S. Camerer, D. König, H. Lorenz, J. P. Kotthaus, and K. Karrai, Optical cooling of a micromirror of wavelength size, Appl. Phys. Lett. **90**, 104101 (2007).
[42] R. A. Barton, I. R. Storch, V. P. Adiga, R. Sakakibara, B. R. Cipriany, B. Ilic, S. P. Wang, P. Ong, P. L. McEuen, J. M. Parpia, and H. G. Craighead, Photothermal self-oscillation and laser cooling of graphene optomechanical systems, Nano Lett. **12**, 4681 (2012).
[43] G. L. Pollack, Kapitza resistance, Rev. Mod. Phys. **41**, 48 (1969).
[44] R. J. Stevens, L. V. Zhigilei, and P. M. Norris, Effects of temperature and disorder on thermal boundary conductance at solid–solid interfaces: Nonequilibrium molecular dynamics simulations, Int. J. Heat Mass Transfer **50**, 3977 (2007).
[45] E. T. Swartz and R. O. Pohl, Thermal boundary resistance, Rev. Mod. Phys. **61**, 605 (1989).
[46] R. E. Peterson and A. C. Anderson, The kapitza thermal boundary resistance, J. Low Temp. Phys. **11**, 639 (1973).
[47] R. M. Costescu, M. A. Wall, and D. G. Cahill, Thermal conductance of epitaxial interfaces, Phys. Rev. B **67**, 054302 (2003).
[48] H.-K. Lyeo and D. G. Cahill, Thermal conductance of interfaces between highly dissimilar materials, Phys. Rev. B **73**, 144301 (2006).
[49] Q.-X. Pei, Y.-W. Zhang, Z.-D. Sha, and V. B. Shenoy, Carbon isotope doping induced interfacial thermal resistance and thermal rectification in graphene, Appl. Phys. Lett. **100**, 101901 (2012).
[50] W. Xu, G. Zhang, and B. Li, Interfacial thermal resistance and thermal rectification between suspended and encased single layer graphene, J. Appl. Phys. **116**, 134303 (2014).
[51] A. Isacsson, A. W. Cummings, L. Colombo, L. Colombo, J. M. Kinaret, and S. Roche, Scaling properties of polycrystalline graphene: A review, 2D Mater. **4**, 012002 (2016).
[52] Y.-C. Wen, C.-L. Hsieh, K.-H. Lin, H.-P. Chen, S.-C. Chin, C.-L. Hsiao, Y.-T. Lin, C.-S. Chang, Y.-C. Chang, L.-W. Tu, and C.-K. Sun, Specular Scattering Probability of Acoustic Phonons in Atomically Flat Interfaces, Phys. Rev. Lett. **103**, 264301 (2009).
[53] A. A. Evans and A. J. Levine, Reflection and Refraction of Flexural Waves at Geometric Boundaries, Phys. Rev. Lett. **111**, 038101 (2013).

[54] J. S. Bunch, S. S. Verbridge, J. S. Alden, A. M. Van Der Zande, J. M. Parpia, H. G. Craighead, and P. L. McEuen, Impermeable atomic membranes from graphene sheets, Nano Lett. **8**, 2458 (2008).

[55] M. Thompson Pettes, I. Jo, Z. Yao, and L. Shi, Influence of polymeric residue on the thermal conductivity of suspended bilayer graphene, Nano Lett. **11**, 1195 (2011).

[56] A. Y. Serov, Z.-Y. Ong, and E. Pop, Effect of grain boundaries on thermal transport in graphene, Appl. Phys. Lett. **102**, 033104 (2013).

[57] S. J. Cartamil-Bueno, A. Centeno, A. Zurutuza, P. G. Steeneken, H. S. Jan van der Zant, and S. Houri, Very large scale characterization of graphene mechanical devices using a colorimetry technique, Nanoscale **9**, 7559 (2017).